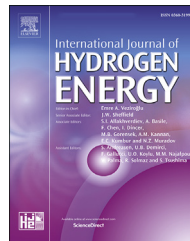




Available online at www.sciencedirect.com
ScienceDirect

journal homepage: www.elsevier.com/locate/he



Robust fault diagnosis and fault tolerant control for PEMFC system based on an augmented LPV observer

Duo Yang, Yujie Wang, Zonghai Chen*

Department of Automation, University of Science and Technology of China, Hefei, 230027, PR China

HIGHLIGHTS

- A LPV model for the PEMFC air management system is proposed.
- An augmented robust observer is designed considering the system noise.
- A fault tolerant control of airflow is proposed.
- The robustness and effectiveness is verified under different fault conditions.

ARTICLE INFO

Article history:

Received 23 September 2019

Received in revised form

9 January 2020

Accepted 9 March 2020

Available online xxx

ABSTRACT

In order to improve the safety and reliability of proton exchange membrane fuel cell system, this paper proposes a novel robust fault observer for the fault diagnosis and reconstruction of the PEMFC air management system. First, considering the complexity and large computation of the nonlinear PEMFC system, a linear parameter-varying (LPV) model is introduced to describe the system behavior and reduce the computation cost. Then, an augmented state observer based on the LPV model is proposed for simultaneously estimating the internal states and component faults. The robustness is guaranteed by taking the system disturbances and measurement noises into consideration when designing the observer gain. The observer design is transformed into a process of solving a set of linear inequality matrices. According to the results, the augmented robust observer can accurately estimate the system states and faults under different conditions. Moreover, to realize the fault tolerant control of the air supply, the oxygen stoichiometry estimator is designed taking consideration of system fault information and a corresponding controller is employed for air compressor voltage following the net power maximization strategy.

© 2020 Hydrogen Energy Publications LLC. Published by Elsevier Ltd. All rights reserved.

Introduction

The proton exchange membrane fuel cell (PEMFC) has become one of the most promising and valued clean energy sources in recent years due to its high specific energy, low operating temperature, low weight, fast start-up, low emissions, etc. The efficiency, reliability and safety have become increasingly important

with the rapid development of PEMFC systems [1,2]. Auxiliary components are essential for the safe and efficient operation of PEMFC. A typical PEMFC system consists of a fuel cell stack, which is made up of a plurality of cells connected in series, an air management system, a hydrogen supply system and a heat exchange system for maintaining a proper stack temperature. Among them, the air management system is a vital subsystem,

* Corresponding author.

E-mail address: chenzh@ustc.edu.cn (Z. Chen).

<https://doi.org/10.1016/j.ijhydene.2020.03.063>

0360-3199/© 2020 Hydrogen Energy Publications LLC. Published by Elsevier Ltd. All rights reserved.

which is used for supplying proper air flow and pressure for the PEMFC stack cathode. Its safe and reliable work plays a crucial role in the performance of fuel cells [3]. However, the nonlinearity, coupling and complexity make it difficult to model and manage.

Accurate modeling is critical for analyzing system characteristics, improving the reliability of the control strategy and ensuring the system security [4]. For control purposes, Pukrushpan et al. [5] proposed the classic 9-order PEMFC nonlinear model, which is widely used for controller and observer design. Ref. [6] built a predictive model based on the Pukrushpan model and used it for predictive control. Xu et al. [7] considered the system uncertainty and modeled the PEMFC by electrochemical method. A simplified mathematical model based on sensors data was proposed for the air supply control in Ref. [8]. The proposed model can be used in real-time applications. Data-driven models are also widely studied, such as neural networks [9], support vector machines (SVMs) [10] and so on. However, this kind of model needs a lot of training data, which is time-consuming and labor-intensive. To make it easier for control, the feedback linearization methods [11] were applied to simply the original nonlinear model and obtain a low-order, linear-form model, and implement the controllers which were designed based on the corresponding models. Additionally, the Takagi-Sugeno (T-S) fuzzy model and the linear parameter-varying (LPV) model are widely applied for building models and observers. Olteanu et al. [12] developed a T-S model for PEMFC system by local linearization, and the accuracy was verified by simulation. Refs. [13,14] proposed T-S fuzzy models for system fault diagnosis. They built observers based on the T-S models and then detected faults by output residual or signal reconstruction. Ref. [15] proposed a time invariant model considering system uncertainty for a robust model predictive control. LPV models, shown in Refs. [16–18], were used for fault diagnosis and reconstruction. Compared to the feedback linearization methods, this kind of methods has lower computation cost and easier to implement, which provides a great convenience for system control and diagnosis.

The fault diagnosis is essential to ensure the safe operation of the fuel cell system. The quantitative fault diagnosis methods of the PEMFC system can be mainly divided into data-driven, signal-based and model-based methods. The signal-based method can be divided into time-domain and frequency-domain methods. Features are extracted from collected signals and compared with preset values to detect faults. For example, Pahon et al. [19] focused on the detection and identification of a high air stoichiometry fault and used the wavelet transform to diagnose fault information. Zheng et al. [20] utilized the electrochemical impedance spectroscopy to analyze the system water fault, and the fuzzy logic was developed to mine the diagnosis rules from the spectrum analysis. Ref. [21] proposed a real-time diagnosis method for PEMFC system based on the stack voltage drop. The signal-based method is simple and intuitive, but it needs a lot of data analysis, and can be hardly applied in real applications. Ref. [22] proposed a sensor selection method to identify faults of a PEMFC system. In terms of the data-driven methods, the fault classifiers based on SVM have been proposed in Refs. [23,24]. This method can identify different stack failure modes by cell voltage generated space. Kim et al. [25]

proposed a hamming neural network for PEMFC state-of-health diagnosis by analyzing the cells voltage. Other methods, such as principal component analysis [26], clustering [27] and deep learning [28] were put forward for judging the fuel cell stack health. The data-driven method can have a good effect on fault classification and prediction of the fuel cell system. Its simplicity and not needing to understand the internal structure make it become potential in fault diagnosis. However, compared to the model-based method, its time-consuming offline training, poor interpretability and sufficient theoretical verification are inconvenient for users [27]. The model-based method is mainly based on the mathematical model, and then utilizes the state observer or filter judge, isolation and reconstruct the fault by residual or fault reconstruction [29]. Refs. [13,30] proposed T-S fuzzy observers to realize the fault estimation and fault tolerant control (FTC). Based on this, an unknown input observer (UIO) was presented considering the sensor faults and disturbance. Ref. [14] considered two mass sensor faults, and presented a UIO and a fault estimator based on an augmented T-S model. Kamal et al. [16] applied a LPV observer for fuel cell fault detection. It detected the system faults by comparing the observer predicted outputs and real measurements. In Ref. [17], the fault diagnosis was realized by structured residuals generation and sensitivity analysis based on a LPV model. Bougatet et al. [18] presented a UIO for the delayed LPV model of the fuel cell system to detect the compressor and outlet orifice faults. And fault isolation was performed using structured residuals. Laghrouche et al. [31] proposed an adaptive-gain second-order sliding mode observer to realize the fault reconstruction for the air supply system. Ref. [32] considered six kinds of faults and proposed a model-based method based on the characterization of the relative residual fault sensitivity. Ref. [33] proposed a robust model-based method based on the super-twisting sliding mode observer to reconstruct the oxygen excess ratio fault. Ref. [34] built two adaptive non-linear observers to diagnose all common faults in a SOFC system. Ref. [35] used an unscented Kalman filter for fuel cell health prognosis. For the model-based method, the difficulty is the acquisition of the analytical model. However, once the system model is determined, this kind of method is the better choice due to the advantages of mature development, high interpretability, and strong robustness. And this kind of method is easier to reconstruct a fault signal rather than merely locate and diagnose, which is helpful for realizing an accurate FTC.

The model-based method is considered for an accurate fault diagnosis in this paper. Aiming at achieving safe and efficient operation of the PEMFC system, we focus on fault diagnosis and reconstruction of possible component failures in the fuel cell air management system and present a FTC for the oxygen stoichiometry regulation. The main contributions of this paper are: (1) A LPV model based on the idea of model fusion for the air management system is proposed. It can simply the nonlinear model simultaneously maintaining a high modeling precision. (2) An augmented robust observer is designed based on the LPV model. The system faults are considered as the augmented states and estimated by real-time state observation. In addition, the proposed observer considers measurement noises and disturbance, which guarantees the robustness and stability of fault diagnosis. (3) A FTC of air flow is proposed based on the oxygen

stoichiometry estimator which takes the fault information into consideration. (4) Simulation experiments under different fault conditions are conducted to verify the robustness and effectiveness of the proposed observer.

The structure of this paper is listed as follows: section [The LPV model of PEMFC air management system](#) introduces the typical air management model and the LPV modeling process. Based on the LPV model, an augmented robust observer is presented in section [The fault diagnosis algorithm](#). In addition, the stability of the observer are proved. The fault estimation method is verified under different conditions in section [The proposed observer application and verification](#). Finally, section [Conclusion](#) gives the conclusion.

The LPV model of PEMFC air management system

In this section, the PEMFC air management system model is introduced. The nonlinear model derived by material conservation and the empirical equation is carried out. Then the LPV model is obtained based on the nonlinear model.

The nonlinear model description

The structure diagram of the PEMFC gas management system is shown in [Fig. 1](#). The air supply part includes an air compressor for a real-time air supply, a supply manifold, a cooler and a humidifier. The exhaust part consists of a return manifold and a backpressure valve used for exhausting the remaining gas and maintaining the stack cathode pressure environment.

In order to characterize the system operating characteristics, a dynamic model based on electrochemical and empirical principles is needed. The cathode flow model follows the law of conservation of mass, as shown in Eq. [\(1\)](#):

$$\begin{cases} \dot{m}_{O_2,ca} = W_{O_2,ca,in} - W_{O_2,ca,out} - W_{O_2,reacted} \\ \dot{m}_{N_2,ca} = W_{N_2,ca,in} - W_{N_2,ca,out} \\ \dot{m}_{w,ca} = W_{w,ca,in} - W_{w,ca,out} + W_{w,ca,gen} + W_{w,membr} \end{cases} \quad (1)$$

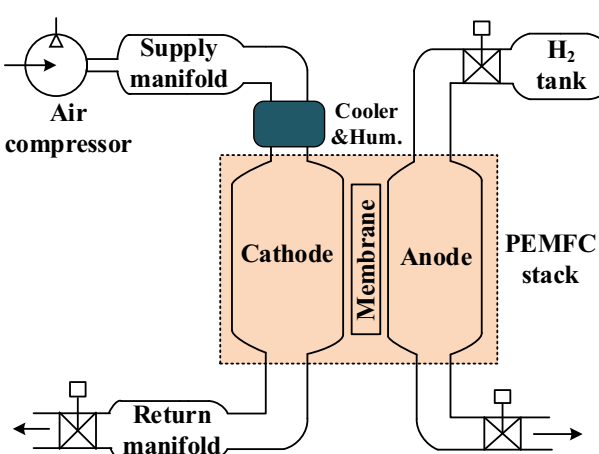


Fig. 1 – The diagram of the PEMFC gas supply system.

where $m_{O_2,ca}$, $m_{N_2,ca}$ and $m_{w,ca}$ are the oxygen mass, nitrogen mass and vapor mass in the cathode; the capital letter W represents the mass flow rate, subscript ca means cathode, and in , out , $reacted$ and gen represent inlet, outlet, electrochemical reaction and product respectively. $W_{w,membr}$ is the vapor mass flow rate transferring across the membrane. The total air mass flow entering the stack cathode $W_{ca,in}$ is the sum of the air mass flow from the supply manifold outlet $W_{sm,out}$ and the mass flow rate of the vapor added by the humidifier $W_{v,hm}$. The air mass flow of the cathode outlet $W_{ca,out}$ is approximately considered as the linear function of the difference between the cathode pressure p_{ca} and the return manifold p_{rm} , as shown in Eq. [\(2\)](#):

$$W_{ca,out} = k_{ca}(p_{ca} - p_{rm}) \quad (2)$$

where k_{ca} is the cathode outlet flow coefficient.

The oxygen flow consumed by the electrochemical reaction and the generated vapor flow are positively correlated with the current I_{st} , as shown in Eq. [\(3\)](#):

$$\begin{cases} W_{O_2,reacted} = M_{O_2} \times \frac{nI_{st}}{4F} \\ W_{v,ca,gen} = M_v \times \frac{nI_{st}}{2F} \end{cases} \quad (3)$$

Suppose the cooler and humidifier are working in an ideal situation, which means the temperature and humidity of the air entering the stack are on the ideal values, then the modeling of air compressor and supply manifold are mainly discussed. The dynamic behavior of the air compressor is modeled as Eq. [\(4\)](#):

$$J_{cp}\dot{\omega}_{cp} = \eta_{cm} \frac{k_t}{R_{cm}} (v_{cp} - k_v \omega_{cp}) - \frac{C_p}{\omega_{cp}} \frac{T_{atm}}{\eta_{cp}} \left[\left(\frac{p_{sm}}{p_{atm}} \right)^{\frac{\gamma-1}{\gamma}} - 1 \right] W_{cp}(p_{sm}, \omega_{cp}) \quad (4)$$

where ω_{cp} represents the motor rotating speed, v_{cp} contributes the input voltage of the compressor, p_{sm} is the air pressure of the supply manifold, $W_{cp}(p_{sm}, \omega_{cp})$ is the air mass flow provided by the air compressor and can be obtained by the map of flow-speed-pressure of air compressor. η_{cp} is the air compressor efficiency. The explanation of other parameters is presented in [Table 1](#).

The model of supply manifold follows the ideal gas state equation, as in Eq. [\(5\)](#):

$$\dot{p}_{sm} = \frac{\gamma R_a}{V_{sm}} (W_{cp} T_{cp,out} - W_{sm,out} T_{sm}) \quad (5)$$

The outlet mass flow $W_{sm,out}$ is calculated by Eq. [\(6\)](#).

$$W_{sm,out} = k_{sm}(p_{sm} - p_{ca}) \quad (6)$$

For the return manifold, the modeling is similar to the supply manifold. Because the temperature does not change much within the pipeline, the temperature variation can be ignored:

$$\dot{p}_{rm} = \frac{T_{rm} R_a}{V_{rm}} (W_{ca,out} - W_{rm,out}) \quad (7)$$

The backpressure valve outlet mass flow $W_{rm,out}$ is determined by the pressure ratio on both sides of the nozzle. The detailed nozzle equation is shown in Ref. [\[5\]](#).

Table 1 – Model parameters of the fuel cell system.

Parameter symbol	Value	Unit	Explanation
n	381	–	Stack cell number
γ	1.4	–	The ratio of the specific heats of air
k_v	0.0153	$V \cdot s \cdot rad^{-1}$	Motor constant
J_{cp}	0.00005	$kg \cdot m^2$	Air compressor inertia
k_t	0.0225	$N \cdot mA^{-1}$	Motor constant
C_p	1004	$J \cdot kg^{-1} \cdot K^{-1}$	Air specific heat capacity at constant volume
t_m	0.01275	cm	Motor constant
R_a	286.9	$J \cdot mol^{-1} \cdot K^{-1}$	Motor constant
k_{sm}	0.363e-5	$kg \cdot s^{-1} Pa^{-1}$	Supply manifold outlet flow coefficient
V_{sm}	0.02	m^3	Supply manifold volume
V_{rm}	0.005	m^3	Return manifold volume
M_{O_2}	32	$g \cdot mol^{-1}$	Oxygen molar mass
M_{N_2}	28	$g \cdot mol^{-1}$	Nitrogen molar mass
M_w	18	$g \cdot mol^{-1}$	Water molar mass
V_{ca}	0.01	m^3	Stack cathode manifold volume
k_{ca}	0.218e-5	$kg \cdot s^{-1} Pa^{-1}$	Cathode outlet flow coefficient
F	96.487	$C \cdot mol^{-1}$	Faraday constant
R_a	8.3145	$J \cdot mol^{-1} \cdot K^{-1}$	Gas constant
T_{fc}	353	K	Stack temperature
T_{atm}	298	K	Ambient temperature

Based on the above equations, the nonlinear state space equation of the whole system can be derived, which is written as the form of Eq. (8):

$$\begin{cases} \dot{\mathbf{x}} = f(\mathbf{x}) + g(\mathbf{x}, \mathbf{u}) \\ \mathbf{y} = C\mathbf{x} \end{cases} \quad (8)$$

where $\mathbf{x} \in \mathbb{R}^{n_x}$ is the state vector, $\mathbf{u} \in \mathbb{R}^{n_u}$ is the input vector, $\mathbf{y} \in \mathbb{R}^{n_y}$. The specific form is:

$\mathbf{x} = [m_{O_2,ca} \ m_{N_2,ca} \ \omega_{cp} \ p_{sm} \ m_{sm} \ p_{rm}]^T$, $\mathbf{y} = [\omega_{cp} \ p_{sm} \ p_{rm}]^T$, $\mathbf{u} = [v_{cp} \ I_{st}]^T$. The every item of state \mathbf{x} respectively represents: the oxygen mass in the stack cathode (g), the nitrogen mass in cathode (g), rotating speed of air compressor (kRPM), the pressure of supply manifold (bar), the air mass in supply manifold (g) and the pressure of return manifold (bar). The specific functions of f and g are as Eq. (9):

$$f(\mathbf{x}) = \begin{bmatrix} \chi_{O_2,in} k_{sm} (x_4 - p_{ca}) - \chi_{O_2,ca} k_{ca} (p_{ca} - x_6) \\ \chi_{N_2,in} k_{sm} (x_4 - p_{ca}) - \chi_{N_2,ca} k_{ca} (p_{ca} - x_6) \\ \frac{1}{J_{cp}} \left(-\eta_{cm} \frac{k_t k_v}{R_{cm}} x_3 - \frac{C_p T_{atm}}{\eta_{cp}} x_3^{-1} \left[\left(\frac{x_4}{p_{atm}} \right)^{\frac{\gamma-1}{\gamma}} - 1 \right] W_{cp}(x_3, x_4) \right) \\ \frac{\gamma R_a}{V_{sm}} [W_{cp}(x_3, x_4) T_{cp,out} - k_{sm} T_{sm}(x_4 - p_{ca})] \\ W_{cp}(x_3, x_4) - k_{sm} (x_4 - p_{ca}) \\ \frac{R_a T_{rm}}{V_{rm}} \left\{ k_{ca} (p_{ca} - x_6) - k_{rm} \left(\frac{p_{atm}}{x_6} \right)^{\frac{1}{\gamma}} \left[1 - \left(\frac{p_{atm}}{x_6} \right)^{\frac{\gamma-1}{\gamma}} \right]^{\frac{1}{\gamma}} \right\} \end{bmatrix}$$

where $\chi_{O_2,in}$ and $\chi_{N_2,in}$ are mass fraction of oxygen and nitrogen of the cathode inlet air, respectively, which can be seen as the mass fraction in the atmospheric environment. $\chi_{O_2,ca}$ and $\chi_{N_2,ca}$ are mass fraction of oxygen and nitrogen in the cathode chamber, which can be calculated by.

$$\chi_{O_2,ca} = \frac{M_{O_2} R_{O_2} T_{fc}}{V_{ca}} x_1 / \left(\frac{M_{O_2} R_{O_2} T_{fc}}{V_{ca}} x_1 + \frac{M_{N_2} R_{N_2} T_{fc}}{V_{ca}} x_2 + M_v p_{sat}(T_{fc}) \right)$$

$$\text{and } \chi_{N_2,ca} = \frac{M_{N_2} R_{N_2} T_{fc}}{V_{ca}} x_2 / \left(\frac{M_{O_2} R_{O_2} T_{fc}}{V_{ca}} x_1 + \frac{M_{N_2} R_{N_2} T_{fc}}{V_{ca}} x_2 + M_v p_{sat}(T_{fc}) \right).$$

p_{ca} is an intermediate variable determined by:

$$p_{ca} = \frac{R_{O_2} T_{fc}}{V_{ca}} x_1 + \frac{R_{N_2} T_{fc}}{V_{ca}} x_2 + \frac{R_v T_{fc}}{V_{ca}} p_{sat}(T_{fc}) \quad (10)$$

R_{O_2} , R_{N_2} and R_v are the gas constants of oxygen, nitrogen and vapor, respectively. we assume the air is always well-humidified and thus the vapor pressure in the cathode is equal to the saturated vapor pressure p_{sat} .

In addition, if the component failure is taken into consideration, the system equation is:

$$\begin{cases} \dot{\mathbf{x}} = f(\mathbf{x}) + g(\mathbf{x}, \mathbf{u}) + h(\mathbf{x}, \mathbf{f}) \\ \mathbf{y} = C\mathbf{x} \end{cases} \quad (11)$$

The fault signal vector $\mathbf{f} \in \mathbb{R}^{n_f}$ is the set of possible component faults, which will be fully discussed in section [The proposed observer application and verification](#).

The LPV model considering fault and disturbance

The LPV model is built based on the idea of multi-model fusion, that is, a set of linear time-invariant models was identified off-line at different operating points, and then the model is obtained by weighting the parameters of the LTI models of different working points.

As the PEMFC system is nonlinear, the model is divided into several parts at different current I_{st} . Taking the fault information and disturbance into consideration, the LPV model can be written as the typical form, as in Eq. (12):

$$\begin{cases} E\mathbf{x}(k+1) = \sum_{i=1}^h \rho_i(\Theta(k)) (G_i\mathbf{x}(k) + H_i\mathbf{u}(k) + F_i\mathbf{f}(k) + D_i\mathbf{w}(k)) \\ \mathbf{y}(k) = C\mathbf{x}(k) + \mathbf{v}(k) \end{cases} \quad (12)$$

where E is a 6-order unit matrix, $\mathbf{w} \in \mathbb{R}^{n_w}$ is the system disturbance, $\mathbf{v} \in \mathbb{R}^{n_v}$ is the system measurement noise. $\Theta(k) \in \Theta$

$$f(\mathbf{x}) = \begin{bmatrix} \frac{n I_{st} M_{O_2} u_2}{4F} \\ 0 \\ \frac{\eta_{cm} k_t u_1}{R_{cm}} \\ 0 \\ 0 \\ 0 \end{bmatrix}, \quad g(\mathbf{x}, \mathbf{u}) = \begin{bmatrix} W_{cp}(x_3, x_4) T_{cp,out} - k_{sm} T_{sm}(x_4 - p_{ca}) \\ W_{cp}(x_3, x_4) - k_{sm} (x_4 - p_{ca}) \\ \frac{R_a T_{rm}}{V_{rm}} \left\{ k_{ca} (p_{ca} - x_6) - k_{rm} \left(\frac{p_{atm}}{x_6} \right)^{\frac{1}{\gamma}} \left[1 - \left(\frac{p_{atm}}{x_6} \right)^{\frac{\gamma-1}{\gamma}} \right]^{\frac{1}{\gamma}} \right\} \end{bmatrix} \quad (9)$$

is a vector of bounded time-varying parameters, and $\rho_i(\theta(k))$, $i = 1, 2, \dots, h$ is the weighting function of $\theta(k)$. The $\theta(k)$ is determined by the current operating points. The weighting function $\rho_i(\theta(k))$ satisfies the following nature:

$$\rho_i(\theta(k)) > 0, \quad \sum_{i=1}^h \rho_i(\theta(k)) = 1 \quad (13)$$

In Eq. (12), the matrices G_i , H_i , and F_i can be obtained by linearizing and discretizing the nonlinear functions $f(\cdot)$, $g(\cdot)$ and $h(\cdot)$ at corresponding operating points, respectively. The dynamic small-signal linearization method is applied in this paper. For the i -th work point, its small-signal model is shown as Eq. (14):

$$\delta\dot{\mathbf{x}} = A_i \delta\mathbf{x} + B_i \delta\mathbf{u} + N_i f \quad (14)$$

where $\delta\mathbf{x} = \mathbf{x} - \mathbf{x}_{o,i}$, $\delta\mathbf{u} = \mathbf{u} - \mathbf{u}_{o,i}$, $\mathbf{x}_{o,i}$ and $\mathbf{u}_{o,i}$ are the steady states and inputs at the i -th work point. $\mathbf{x}_{o,i}$ is denoted by calculating the nonlinear model Eqs. (1)–(7) at the operating point. And the matrices A_i , B_i and N_i are calculated by the direct linearization of the nonlinear model [12]. The calculation equations are: $A_i = \left. \frac{\partial f(\cdot)}{\partial \mathbf{x}} \right|_{(\mathbf{x}_{o,i}, \mathbf{u}_{o,i})}$, $B_i = \left. \frac{\partial g(\cdot)}{\partial \mathbf{u}} \right|_{(\mathbf{x}_{o,i}, \mathbf{u}_{o,i})}$ and $N_i = \left. \frac{\partial h(\cdot)}{\partial \mathbf{f}} \right|_{(\mathbf{x}_{o,i}, \mathbf{u}_{o,i})}$.

Rewrite Eq. (14) as:

$$\begin{aligned} \dot{\mathbf{x}} &= A_i(\mathbf{x} - \mathbf{x}_{o,i}) + B_i(\mathbf{u} - \mathbf{u}_{o,i}) + N_i f \\ &= A_i \mathbf{x} + B_i \mathbf{u} + N_i f - (A_i \mathbf{x}_{o,i} + B_i \mathbf{u}_{o,i}) \end{aligned} \quad (15)$$

where $-(A_i \mathbf{x}_{o,i} + B_i \mathbf{u}_{o,i})$ is a constant vector. Label it as a constant item M_i . Since M_i can be obtained off-line, it can also be considered as a known input disturbance. Eq. (15) can be rewritten as:

$$\dot{\mathbf{x}} = A_i \mathbf{x} + B'_i \mathbf{u}' + N_i f \quad (16)$$

where $B'_i = [B_i \ M_i]$, $\mathbf{u}' = [v_{cp} \ I_{st} \ 1]^T$. Through the

discretization process, the matrices G_i , H_i and F_i in Eq. (12) are obtained from A_i , B'_i and N_i , respectively.

The matrix D_i in Eq. (12) represents a system disturbance matrix. Normally, the disturbance means some unmeasured information, including system noise, nonlinear model errors, and errors caused by linearization, etc. In order to reduce the influence of the disturbance in state estimation and prevent fault misjudgment caused by model error and other factors, we introduce the disturbance matrix D_i , and a reasonable robust observer is needed to improve the robustness of fault diagnosis. For these unmeasurable noises which are often difficult to be obtained, the disturbance matrix is generally set by experience.

Assumptions.

A1. The matrix C is of full row rank. And E and C satisfy:

$$\text{rank} \begin{bmatrix} E \\ C \end{bmatrix} = n_x.$$

A2. The matrices F_i , $i = 1, \dots, h$, are of full column rank.

The system model satisfies the Assumptions, and the corresponding verification process is shown in Appendix.

The fault diagnosis algorithm

For the LPV system Eq. (12), an augmented LPV observer is built for fault estimation. The idea is to consider the faults as additional state variables, and construct an augmented system through the state augmentation, then design a corresponding observer to realize fault reconstruction. In Refs. [18,30], the augmented system has been proposed. However, in these kinds of literatures, the augmented system was designed with the assumption that the fault signal remains unchanged in a sampling interval. In this paper, this problem

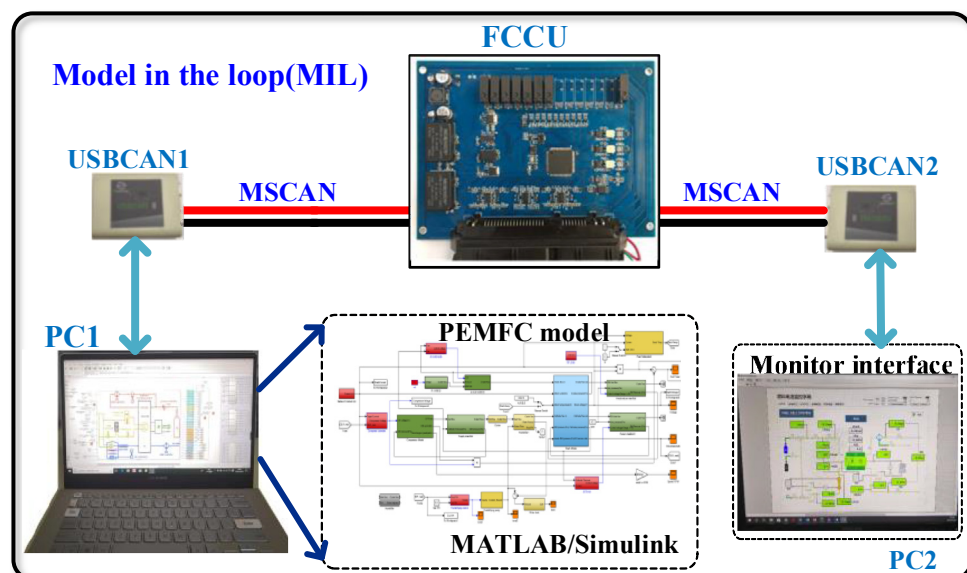


Fig. 2 – The MIL test bench.

is avoided by improving the structure of the observer, as shown in Eq. (17):

$$\begin{cases} \bar{E}\bar{x}(k+1) = \sum_{i=1}^h \rho_i(\theta(k))(\bar{G}_i\bar{x}(k) + \bar{H}_i u(k) + \bar{D}_i w(k) + \bar{K}_i \Delta f(k)) \\ y(k) = \bar{C}\bar{x}(k) + v(k) \end{cases} \quad (17)$$

where

$$\bar{x}(k) = \begin{bmatrix} x(k) \\ f(k) \end{bmatrix}, \Delta f(k) = f(k+1) - f(k)$$

$$\bar{E} = \begin{bmatrix} E & 0 \\ 0 & I_{n_f} \end{bmatrix}, \bar{G}_i = \begin{bmatrix} G_i & F_i \\ 0 & I_{n_f} \end{bmatrix}, \bar{H}_i = \begin{bmatrix} B_i \\ 0 \end{bmatrix}, \bar{D}_i = \begin{bmatrix} D_i \\ 0 \end{bmatrix}, \bar{K}_i = \begin{bmatrix} 0 \\ I_{n_f} \end{bmatrix}, \bar{C} = [C_0]$$

Based on Eq. (17), a robust fault diagnosis observer is designed in Eq. (18):

$$\begin{cases} \zeta(k+1) = \sum_{i=1}^h \rho_i(\theta(k))(T\bar{G}_i\hat{x}(k) + T\bar{H}_i u(k) + L_i(y(k) - \bar{C}\bar{x}(k))) \\ \hat{x}(k) = \zeta(k) + Ny(k) \end{cases} \quad (18)$$

where $\zeta(k) \in \mathbb{R}^{(n_x+n_f)}$ is an intermediate variable, $\bar{x}(k) \in \mathbb{R}^{(n_x+n_f)}$ is the estimate of the augmented state $\bar{x}(k)$. $T \in \mathbb{R}^{(n_x+n_f) \times n_x}$, $N \in \mathbb{R}^{(n_x+n_f) \times n_u}$ and $L_i \in \mathbb{R}^{(n_x+n_f) \times n_u}$, $i = 1, \dots, h$ are matrices needed to be determined.

Lemma 1. If the assumption A2 is satisfied, then there exists a non-singular matrix T and a matrix N , which satisfy:

$$T\bar{E} + N\bar{C} = I_{n_x+n_f} \quad (19)$$

According to Lemma 1, the general solution of T and N can

$$[TN] = \left[\frac{\bar{E}}{C} \right]^+ + S \left(I_{n_x+n_f+n_u} - \left[\frac{\bar{E}}{C} \right] \left[\frac{\bar{E}}{C} \right]^+ \right) \quad (20)$$

where $S \in \mathbb{R}^{(n_x+n_f+n_u) \times (n_x+n_f+n_u)}$ is an arbitrary matrix.

Label $\left[\frac{\bar{E}}{C} \right]$ as Ψ , then T and N can be determined by:

$$T = \Psi^+ \alpha_1 + S \left(I_{n_x+n_f+n_u} - \Psi \Psi^+ \right) \alpha_1 \quad (21)$$

$$N = \Psi^+ \alpha_2 + S \left(I_{n_x+n_f+n_u} - \Psi \Psi^+ \right) \alpha_2 \quad (22)$$

$$\text{where } \alpha_1 = \begin{bmatrix} I_{n_x+n_f} \\ 0 \end{bmatrix}, \alpha_2 = \begin{bmatrix} 0 \\ I_{n_u} \end{bmatrix}.$$

The error function can be derived by Eqs. 17–19:

$$\begin{aligned} \mathbf{e}(k+1) &= \bar{x}(k+1) - \hat{x}(k+1) = T\bar{E}\bar{x}(k) - \zeta(k) - Nv(k+1) \\ &= \sum_{i=1}^h \rho_i(\theta(k))((T\bar{G}_i - L_i\bar{C})\mathbf{e}(k) + T\bar{D}_i w(k) + T\bar{K}_i \Delta f(k) - L_i v(k) \\ &\quad - Nv(k+1)) \end{aligned} \quad (23)$$

As in Eq. (23), if the disturbance, fault and measurement noise are bounded, and the observer gain L_i is designed properly, the system error is convergent and bounded. The gain L_i can be solved by solving the linear matrix inequalities (LMIs) in Theorem 1.

Theorem 1. For the augmented LPV system Eq. (17) and the given scalars $\gamma_d > 0$, $\gamma_f > 0$, $\gamma_{v1} > 0$, $\gamma_{v2} > 0$, if there exists a symmetric positive definite matrix $P \in \mathbb{R}^{(n_x+n_f) \times (n_x+n_f)}$ and a matrix $W_i \in \mathbb{R}^{(n_x+n_f) \times n_u}$, $i = 1, \dots, h$, satisfying:

$$\left[\begin{array}{cccccc} -P + C_f^T C_f & 0 & 0 & 0 & 0 & \mathcal{G}_{1i}^T P + \mathcal{G}_{1i}^T S^T P - \bar{C}^T W_i^T \\ * & -\gamma_d^2 I_{n_x} & 0 & 0 & 0 & \mathcal{D}_{1i}^T P + \mathcal{D}_{2i}^T S^T P \\ * & * & -\gamma_f^2 I_{n_f} & 0 & 0 & \mathcal{K}_{1i}^T P + \mathcal{K}_{2i}^T S^T P \\ * & * & * & -\gamma_{v1}^2 I_{n_u} & 0 & -W_i^T \\ * & * & * & * & -\gamma_{v2}^2 I_{n_u} & -\mathcal{N}_1^T P - \mathcal{N}_1^T S^T P \\ * & * & * & * & * & -P \end{array} \right] < 0, \quad i = 1, 2, \dots, h \quad (24)$$

be determined by:

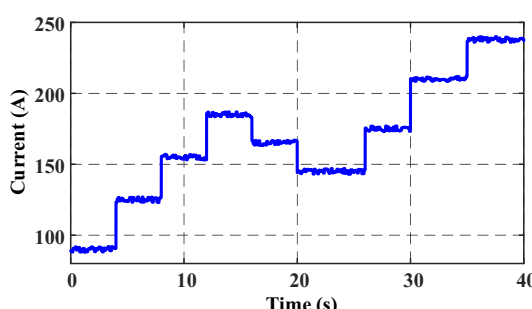


Fig. 3 – The step current profile conducted on the PEMFC system.

where $C_f \in \mathbb{R}^{n_f \times (n_x+n_f)}$ is defined as $C_f = [0I_{n_f}]$, and then the fault estimation value can be obtained by $\hat{f}(k) = C_f \bar{x}(k)$. Then matrices \mathcal{G}_{1i} , \mathcal{D}_{1i} , \mathcal{K}_{1i} and \mathcal{N}_1 are:

$$\mathcal{G}_{1i} = \Psi^+ \alpha_1 \bar{G}_i, \quad \mathcal{G}_{2i} = \left(I_{n_x+n_f+n_u} - \Psi \Psi^+ \right) \alpha_1 \bar{G}_i \quad (25)$$

$$\mathcal{D}_{1i} = \Psi^+ \alpha_1 \bar{D}_i, \quad \mathcal{D}_{2i} = \left(I_{n_x+n_f+n_u} - \Psi \Psi^+ \right) \alpha_1 \bar{D}_i \quad (26)$$

$$\mathcal{K}_{1i} = \Psi^+ \alpha_1 \bar{K}_i, \quad \mathcal{K}_{2i} = \left(I_{n_x+n_f+n_u} - \Psi \Psi^+ \right) \alpha_1 \bar{K}_i \quad (27)$$

$$\mathcal{N}_1 = \Psi^+ \alpha_2, \quad \mathcal{N}_2 = \left(I_{n_x+n_f+n_u} - \Psi \Psi^+ \right) \alpha_2 \quad (28)$$

Then the error function $e_f(k) = f(k) - \hat{f}(k)$ is robust to

process disturbances, fault changes, and measurement noise, which can be expressed by:

$$\|\mathbf{e}_f\|_2 \leq \sqrt{\gamma_d^2 \|\mathbf{w}\|_2^2 + \gamma_f^2 \|\Delta \mathbf{f}\|_2^2 + (\gamma_{v1}^2 + \gamma_{v2}^2) \|\mathbf{v}\|_2^2 + V(0)} \quad (29)$$

where $\|\cdot\|_2$ represents the 2-norm, $V(0)$ is a quadratic function of $\mathbf{e}(0)$, which will be introduced in the next part. If the LMIs shown in Eq. (24) have a solution, the observer gain L_i is determined by:

$$L_i = P^{-1} W_i, \quad i = 1, 2, \dots, h \quad (30)$$

The verification process of Theorem 1 is shown in the Appendix part.

The proposed observer application and verification

In this case, in order to verify the performance of the proposed observer, the vehicle 75 kW fuel cell system is applied. Section [The nonlinear model description](#) introduces its air supply system model, which is derived from the typical Pukrushpan model [5]. The main parameters of this fuel cell system are shown in [Table 1](#).

The model in the loop (MIL) test in [Fig. 2](#) is applied to conduct the simulation experiments. The PEMFC model is built under the Matlab/Simulink environment. The FCCU in the figure is the master control unit, which is used for parameter acquisition and relay control for fuel cell system. The Freescale MC9S12XEP100 is selected as the main control chip. In the MIL test, the proposed observer is designed offline and integrated into the control board for fault diagnosis. The real-time communication between computers and FCCU is carried out by CAN protocol.

The key parameters determination of the augmented LPV observer

As discussed in section [The LPV model of PEMFC air management system](#), the proposed model is determined by the sub-model at each operating point. The fuel cell current is

normally from 80A to 300A. Taking into account the complexity and precision of the model, from the current of 90A, select one working point every 30A interval until the current reaches 270A. The sub-model at each operating point is obtained off-line through Eq. (14). Then we obtained the weight factor of the linear model at each working point according to the distance between the current value of the system and the set working point. The weight factor $\rho_i(\theta(k))$ is determined by the linear interpolation method. In addition, the working behavior when current is less than 90A or higher than 270A is totally determined by the sub-model at 90A or 270A, respectively. The final LPV model is obtained by the weighted summation of these sub-models.

Furthermore, it is necessary to obtain prior knowledge of the fault information, as the $h(\mathbf{x}, \mathbf{f})$ function in Eq. (11). In this case, we consider two common faults of components in the air supply system: the supply manifold fault (pipeline gas leaks or blockage) and the backpressure valve fault (valve opening deviation), which are respectively labeled as f_1 and f_2 . It is worth mentioning that a single observer cannot identify all component failures because the state quantity of the augmented model increases with the increase of the fault information, which leads to the system being unobservable. Therefore, we perform state observations at two key components of the system to reconstruct the corresponding faults. The relationship between the faults and the system states is established through model analysis to obtain the fault model $h(\mathbf{x}, \mathbf{f})$. The corresponding linearized matrix F_i is shown in Appendix. The matrices $[\bar{G}_i \ C]$, $i = 1, \dots, h$ are proven to be of full row rank, which indicates the augmented system is observable.

Additionally, matrices T , N , and S are needed before solving L_i . First, according to Theorem 1, the solution of L_i is related to S . Theorem 1 can also be applied by considering the matrix S as an unknown matrix to be solved, the same as matrix P and W_i . However, this will result in a large calculation. In this case, the matrix S is pre-set. Choose $S = [I_{n_x+n_f} \ 0_{(n_x+n_f) \times n_u}]$, then T and N are solved by Eqs. (21) and (22). The disturbance matrix D_i , $i = 1, \dots, h$ is also needed to be determined. As discussed in section [The LPV model considering fault and disturbance](#), the

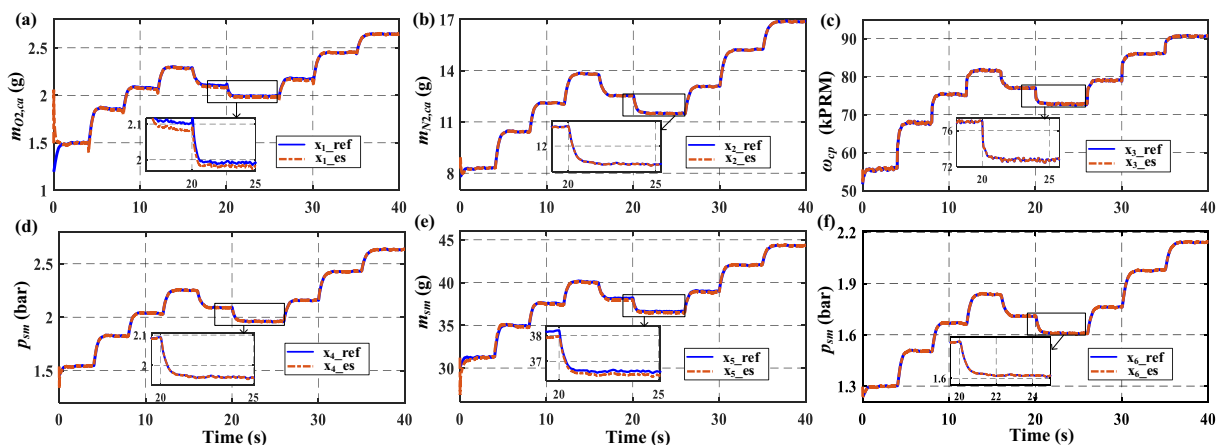


Fig. 4 – The estimation results of states: (a) Cathode oxygen mass. (b) Cathode nitrogen mass. (c) Compressor speed. (d) Pressure in supply manifold. (e) Air mass in supply manifold. (f) Pressure in return manifold.

matrix D_i is designed as a diagonal matrix, and the value of each point on the diagonal is designed by the magnitude of the corresponding internal states.

The fault estimation results description

The proposed observer is verified in this section. In order to make the experimental results sufficiently convincing, a step current profile basically covering the full working range is applied shown in Fig. 3. In addition, a small range (within 2A) of random noise is applied to the current to simulate the disturbances in the actual operating conditions. The current noise is set based on the similar method in Ref. [38], which can generally represent the noise in the stable step profile of a PEMFC system. On the other hand, in order to show the robustness of the observer, and simulate the real working environment, the measurement noise, which is the vector \mathbf{v} in Eq. (12), is added. The measurement noises are zero mean white noise signals.

Case 1: The fuel cell system is working when no fault occurs.

The state values estimated by the proposed observer under the situation of no fault are shown in Fig. 4. It can be seen from the figure that the proposed method can accurately estimate the states of the system, and it is also proved that the augmented fault states have little effect on the original state estimation.

In order to more intuitively represent system fault information, we use the additional air flow increase/decrease caused by the pipeline or valve faults as the fault signals and reconstruct them. The fault reconstruction results are shown in Fig. 5. Fig. 5(a) and (b) respectively show the estimation results of the f_1 and f_2 in the case of no fault. In this case, the results of the fault estimate should be 0. The fault reference value is shown by the solid blue line in the figure. The interval shock occurs in the fault estimation, which is caused by larger current fluctuation. This is difficult to be avoided because of the system inertia and observer delay. However, this situation doesn't affect the judgment of whether the system is faulty, because the estimated value will immediately return to the reference value after the end of the sudden change of current. Additionally, during the current stagnation phase, the estimates also occasionally have deviations, which are caused by modeling errors. Deviations can be reduced by designing the reasonable disturbance matrix D_i , but they cannot be completely eliminated. This deviation doesn't affect our judgment of system fault, either. First, the magnitude of this deviation is less than the true fault value. Second, this deviation does not persist. When the system jumps to another working point, the deviation may disappear or become extremely small.

Case 2: Fault occurs on the supply manifold ($f_1 \neq 0$, $f_2 = 0$).

In case 2, we assume a fault signal on the supply manifold in order to verify the proposed method. First, assume that a

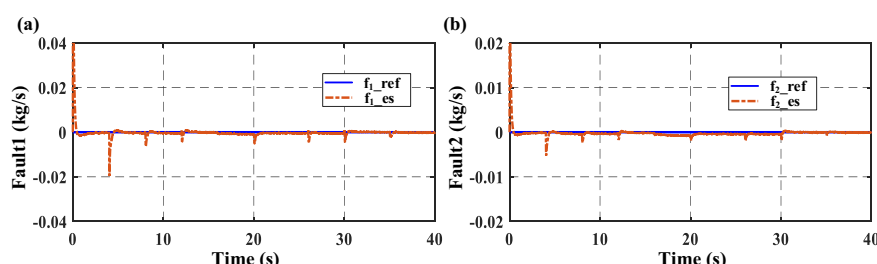


Fig. 5 – The fault estimation results under case 1. (a) The estimation result of f_1 . (b) The estimation result of f_2 .

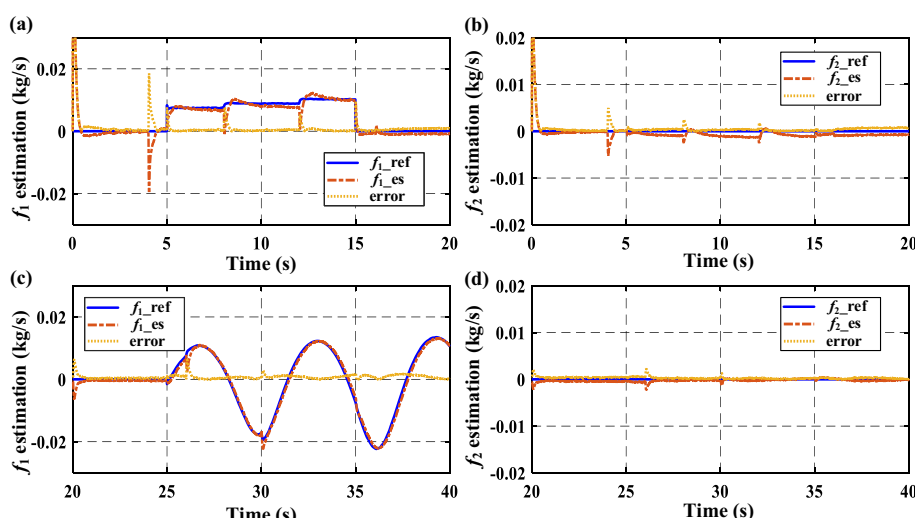


Fig. 6 – The fault estimation results under case 2: (a) f_1 with a step fault. (b) f_2 with a step fault. (c) f_1 with a sinusoidal fault. (d) f_2 with a sinusoidal fault.

step fault signal appears at 5s as shown in Fig. 6(a)-(b). This fault is simulated by the supply pipeline outlet valve coefficient change. Furthermore, we use another dynamic fault for further confirmation. In this case, a sinusoidal signal is added in the supply manifold outlet coefficient around 25s, as shown in Fig. 6(c)-(d). From the figure, the f_1 estimation value can track the real value well. Meanwhile, the f_2 estimate value basically remains unchanged, which indicates that there is good independence between the two faults and they do not affect each other. The yellow dot curves in the figures are the estimation error calculated by the difference between the reference value and the estimated value.

Case 3: Fault occurs on the outlet backpressure valve ($f_1 = 0$, $f_2 \neq 0$).

Case 3 considers the situation that a fault occurs on the backpressure valve, that is, $f_2 \neq 0$. Same as case 2, a step fault is

considered. Assume the valve is partially blocked at 25s, then fault estimation results are shown in Fig. 7(a)-(b). In addition, a ramp fault signal is used for simulating the slowly changing faults in the back pressure valve, as Fig. 7(c) shows. The deviations that occur in the fault estimate are due to model deviations. The error is small relative to the magnitude of the fault, so the system fault information can still be correctly judged.

Case 4: Faults occur on both locations ($f_1 \neq 0$, $f_2 \neq 0$).

Finally, we consider the situation that f_1 and f_2 occur at the same time. Two conditions are simulated. Fig. 8 (a)-(b) display the faults estimation results where f_1 is a step fault and f_2 is a ramp fault. f_2 occurs at 12s, and f_1 occurs at 20s when f_2 is happening. Fig. 8 (c)-(d) display another condition that f_1 is a sinusoidal signal and f_2 is a step signal. The estimation results under the two situations both show that the estimation is

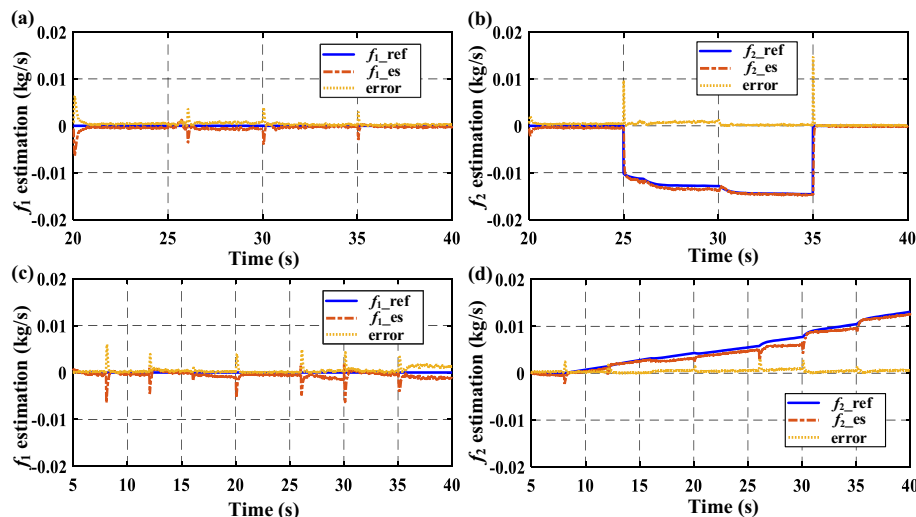


Fig. 7 – The fault estimation results under case 3: (a) f_1 with a step fault. (b) f_2 with a step fault. (c) f_1 with a ramp fault. (d) f_2 with a ramp fault.

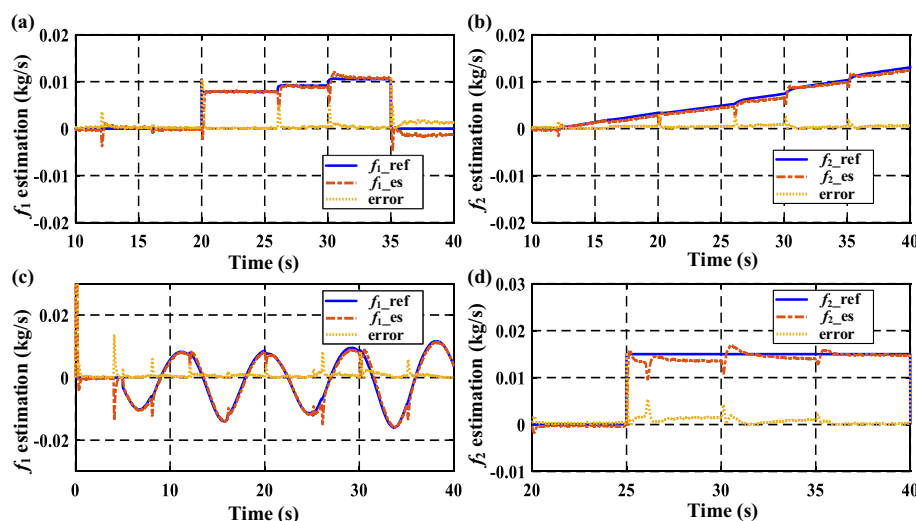


Fig. 8 – The fault estimation results under case 4. (a) f_1 estimation with f_1 a step fault and f_2 a ramp fault. (b) f_2 estimation with f_1 a step fault and f_2 a ramp fault. (c) f_1 estimation with f_1 a sinusoidal fault and f_2 a step fault. (d) f_2 estimation with f_1 a sinusoidal fault and f_2 a step fault.

accurate when faults occur simultaneously. The repetitive and fairly large magnitude errors which appear in yellow curves in Figs. 6–8 are caused by the large current profile variation. The system parameters change greatly in a short time when the load has a large change, and the state tracking of the observer has a delay, so the observation results will also have a large deviation at this time. However, the delay is small, and the result of fault estimation can quickly recover to the real value.

Accuracy evaluation and comparison of the fault estimation methods

For showing the superiority of the proposed method, we introduce another widely-used observer: the UIO to make a comparison. However, the UIO in Ref. [18] did not consider the disturbance and noise, which makes it cannot estimate faults effectively in the context of this study. So the optimal unknown input observer (OUIO) is applied to improve the performance of UIO. The OUIO is a real-time iterative algorithm, its principle is shown in Ref. [37]. We take a sinusoidal fault for an example, the results comparison of the OUIO and the proposed LPV observer is shown in Fig. 9. According to the results, the proposed observer shows higher accuracy than the OUIO.

The root mean square error (RMSE) and mean absolute error (MAE) are applied to describe the model accuracy in a quantitative way. Table 2 shows the values of RMSEs and MAEs of the proposed method and the OUIO. In Table 2, case 2_1 and case 2_2 represent the first (as Fig. 5(a) (b) show) and second (as Fig. 5(c) (d) show) situation in case 2, respectively, and the meanings of other items are analogous.

In addition, another comparison group is shown to illustrate the robustness to noise of the proposed method. In the

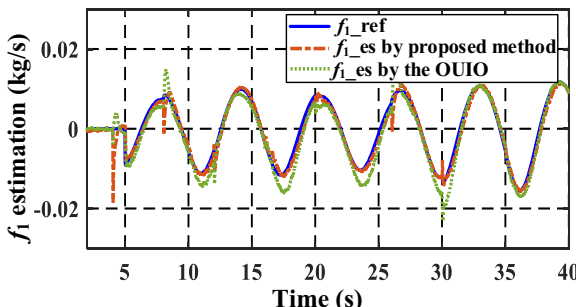


Fig. 9 – The estimation results comparison of the mentioned methods.

previous experiments, the measurement noises are set small, and the order of magnitude is set to 0.1 kPa of the pressure measurement noise. In this part, we amplify the noise of measurement signal to the order of 1 kPa to show whether the observer can deal with the noises well. The comparison results of the proposed observer and the OUIO under large noises are shown in Fig. 10. Both methods also can estimate faults under this condition. However, from the results, the LPV observer shows much better estimation accuracy and higher robustness. And the results by the proposed method show smaller oscillation, which indicates the proposed observer can deal with noises more effectively. Also apparently, as the noise continues to increase, ultimately the observer cannot operate effectively because too much noise indicates that the sensor is invalid and cannot get enough effective information from the measured data.

The fault tolerant control of air supply system

The oxygen stoichiometry is a key indicator in the fuel cell system, which is defined as the ratio of the oxygen mass flow required for electrochemical reactions and the actual oxygen mass flow supplied by the air compressor [36]. It is important to control the oxygen stoichiometry at a proper value where the fuel cell system can maintain both high performance and safety. However, the oxygen stoichiometry is unmeasurable and has to be estimated indirectly. Considering the system faults, it is calculated by Eq. (36):

$$\hat{\lambda}_{O_2} = \frac{\widehat{W}_{O_2,ca,in}}{\widehat{W}_{O_2,reacted}} = \frac{\widehat{W}_{O_2,ca,in,r} + \widehat{W}_{O_2,ca,in,f}}{\widehat{W}_{O_2,reacted}} = a_1 \frac{\widehat{p}_{sm} - \widehat{p}_{ca}}{I_{st}} + a_2 \frac{\widehat{f}_1}{I_{st}} \quad (31)$$

where a_1 and a_2 are constant coefficients, and $a_1 = \frac{x_{O_2,atm}k_{sm}}{(1+\omega_{atm})nM_{O_2}/4F}$, $a_2 = \frac{x_{O_2,atm}}{(1+\omega_{atm})nM_{O_2}/4F}$. $x_{O_2,atm}$ is the volume fraction of oxygen in the atmosphere, ω_{atm} is the humidity ratio of the environment. The estimate of stack cathode pressure \widehat{p}_{ca} is obtained by the oxygen and nitrogen partial pressure estimates in the cathode, as shown in Eq. (37):

$$\widehat{p}_{ca} = \widehat{p}_{O_2,ca} + \widehat{p}_{N_2,ca} + p_{v,ca} = c_1 \widehat{x}_1 + c_2 \widehat{x}_2 + p_{v,ca} \quad (32)$$

where \widehat{x}_1 and \widehat{x}_2 are the first and second items of the system \mathbf{x} , that is, $m_{O_2,ca}$ and $m_{N_2,ca}$. c_1 and c_2 are constants: $c_1 = \frac{\gamma R_{O_2}}{V_{ca}}$, $c_2 = \frac{\gamma R_{N_2}}{V_{ca}}$. $p_{v,ca}$ is the vapor pressure in the cathode, and it is considered as the saturated vapor pressure according to section **The LPV model of PEMFC air management system**.

The λ_{O_2} controller consists of a static feedforward controller and a feedback controller. The SFF controller is

Table 2 – The RMSEs and MAEs of the proposed method and the OUIO method.

Item	Error index	Method	Case 2_1	Case 2_2	Case 3_1	Case 3_2	Case 4_1	Case 4_2
f_1	RMSE(kg/s)	Proposed	1.343e-3	1.229e-3	1.070e-3	1.219e-3	1.634e-3	2.567e-3
		OUIO	2.207e-3	2.240e-3	1.160e-3	1.808e-3	3.541e-3	3.560e-3
	MAE(kg/s)	Proposed	7.233e-4	7.119e-4	5.418e-4	7.141e-4	9.652e-4	1.600e-3
		OUIO	1.673e-3	1.645e-3	9.485e-4	1.559e-3	2.356e-3	2.547e-3
f_2	RMSE(kg/s)	Proposed	6.751e-4	5.225e-4	7.078e-4	7.324e-4	9.039e-4	1.443e-3
		OUIO	9.960e-4	9.975e-4	7.189e-4	9.140e-4	1.378e-3	1.702e-3
	MAE(kg/s)	Proposed	5.053e-4	3.835e-4	3.990e-4	5.836e-4	6.664e-4	8.908e-4
		OUIO	7.690e-4	7.460e-4	4.955e-4	7.703e-4	9.597e-4	1.186e-3

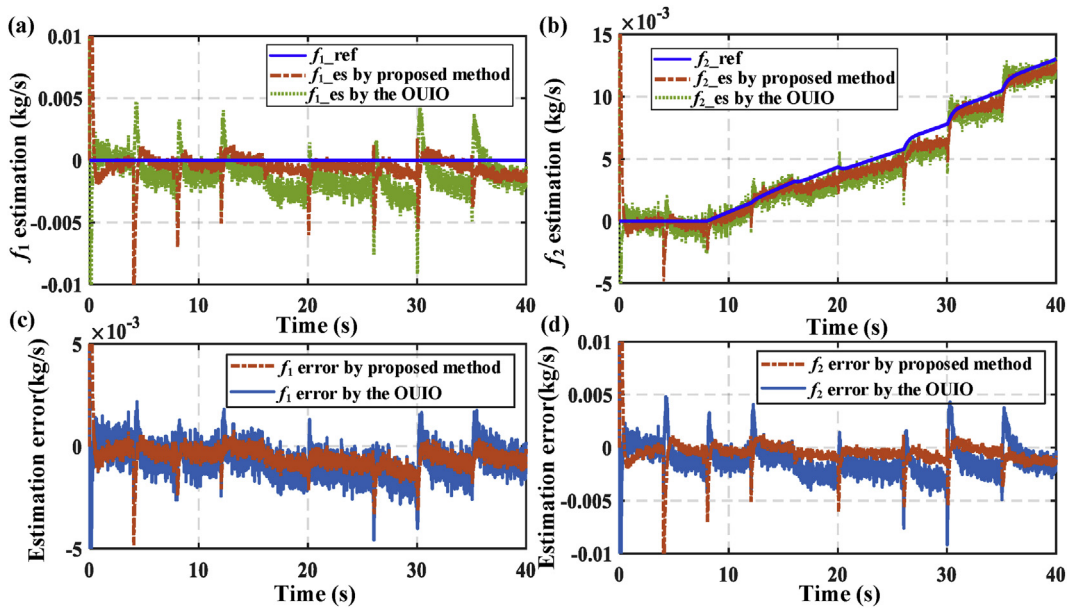


Fig. 10 – The estimation results comparison of the mentioned methods considering a high sensor error. (a) The f_1 estimation with f_2 a ramp fault. (b) The f_1 estimation error. (c) The f_2 estimation with f_2 a ramp fault. (d) The f_2 estimation error.

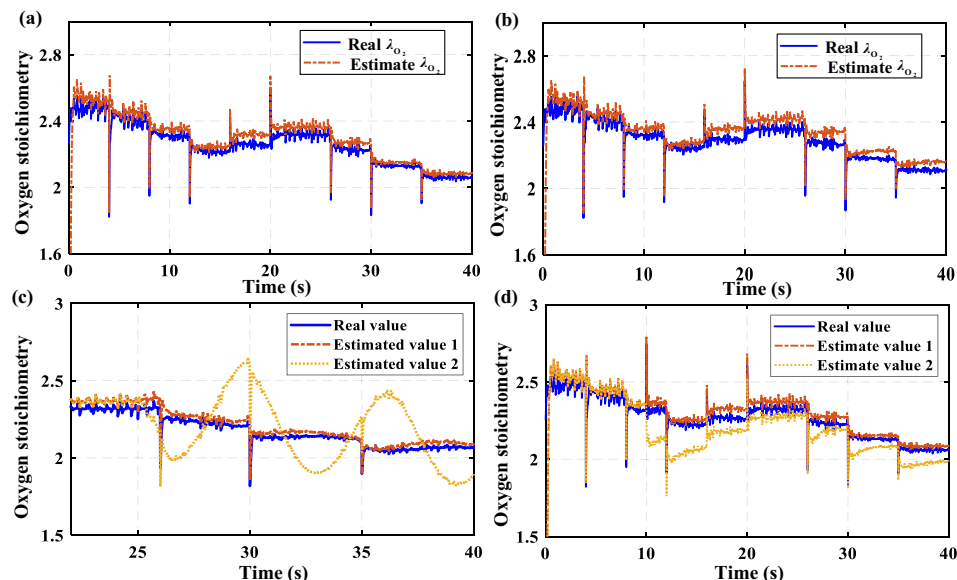


Fig. 11 – (a) The λ_{O_2} estimation results when system is healthy. (b) The λ_{O_2} results when f_2 is a ramp fault at 8s. (c) The λ_{O_2} estimation results when f_1 is a sinusoidal fault at 25s. (d) The λ_{O_2} estimation results when f_1 is a step fault at 10s.

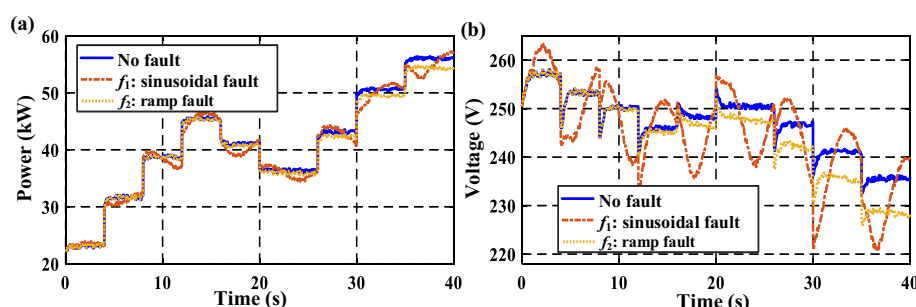


Fig. 12 – System output performance. (a) The system power. (b) The output voltage.

designed off-line by testing the optimal compressor voltage at different working points. The so-called optimal compressor voltage is the operating voltage when the λ_{O_2} reaches the ideal value. The feedback controller tries to minimize the error between the ideal control goal and the actual value. The governor defines the ideal λ_{O_2} value at different current by off-line test, which is designed for maximizing the system net power [11].

Based on the profile as Figs. 3 and 11(a) shows estimation results under case 1. Fig. 11 (b) shows the results when f_2 is a ramp fault. The jitter of the curve is caused by current variation, system noise and the state variation. The estimation error is due to the state estimation error. The performance of the fault tolerant controller is shown in Fig. 11(c) and (d). Fig. 11(c) and (d) respectively display the results under a sinusoidal fault and a constant deviation fault on the supply manifold (case 2). The yellow dotted line in figures is the $\hat{\lambda}_{O_2}$ value without considering the system fault information. The red line is the $\hat{\lambda}_{O_2}$ value obtained by Eq. (35). It is obvious that the yellow curves may not track the real value when a fault occurs. This situation is likely to cause serious consequence. For example, the wrong $\hat{\lambda}_{O_2}$ may cause inappropriate control voltage by the feedback controller, which may lead to the system working in an abnormal working point, and even jeopardize the stack health.

The system performance analysis

In addition, we show the influence on system output performance when the fault occurs and inappropriate control effect. The output performance mainly refers to output voltage and power. The terminal voltage and output power of the PEMFC stack can be modeled as Eqs. (33) and (34):

$$V_{st} = nV_{cell} \quad (33)$$

$$P_{st} = V_{st}I_{st} \quad (34)$$

where n is the cell number, V_{cell} is the voltage of a single cell. V_{cell} is calculated by subtracting the voltage loss terms from the Nernst voltage E , as shown in Eq. (35).

$$V_{cell} = E - V_{act} - V_{ohm} - V_{conc} \quad (35)$$

The Nernst voltage E is obtained by Eq. (36):

$$E = 1.428 - 8.45 \times 10^{-4}T_{fc} + 4.31 \times 10^{-5}T_{fc} \left(\ln \frac{p_{H_2}}{1.01325} + \frac{1}{2} \ln \frac{p_{O_2}}{1.01325} \right) \quad (36a)$$

where p_{H_2} and p_{O_2} are the partial pressure of hydrogen and oxygen in the stack.

V_{act} , V_{ohm} and V_{conc} denote the activation loss, ohmic loss and concentration loss in Eq. (35) respectively, and they are obtained by Eqs. 36–38:

$$V_{act} = v_0 + v_a(1 - e^{-c_1 i}) \quad (36b)$$

$$V_{ohm} = i \cdot R_{ohm} \quad (37)$$

$$V_{conc} = i \left(c_2 \frac{i}{i_{max}} \right)^{c_3} \quad (38)$$

where v_0 , v_a , c_1 , c_2 and c_3 are empirical parameters. R_{ohm} is the ohmic resistance. i is the current density. The specific expression of R_{ohm} and parameters are listed in Ref. [5].

Actually, the two faults in this paper represent the abnormal air flow variation in the PEMFC system. According to the above calculation process, the electric performance of the fuel cell system is shown in Fig. 12. The solid blue lines show the output power and voltage in case 1. The red lines show the performance curves when there is a sinusoidal fault in supply manifold at initial time. Similarly, the yellow dot lines show the output capability when a ramp fault occurs in f_2 at 8s. It can be seen that the sinusoidal fault in f_1 causes large fluctuation on the system voltage and power. The ramp fault in f_2 causes the system performance decrease. The larger faults cause larger performance degradation, in serious cases, it will damage system security. In the condition shown in this figure, the maximum power variation can reach to 8% (about 4 kW), which is a big effect on the output performance. Furthermore, the unstable and reduced performance caused by the two faults is difficult to control. As shown in Fig. 11, the faults will influence the estimation of the system oxygen stoichiometry, which has a serious influence on air flow control, as discussed in section The fault tolerant control of air supply system.

Finally, the time cost of the proposed observer is discussed. The time cost is low because the complicated process of the LPV observer gain determination is obtained offline. Once the gain is determined, the observer can be used to estimate fault in real time. What takes time cost in real-time operation is the real-time acquisition of parameters of LPV model and the feedback calculation of observer itself, whose calculation cost are relatively low. The average time cost of each execution time is 1.79 ms by simulation experiments.

Conclusion

In this paper, an augmented LPV observer is proposed for the high-precision state estimation and fault reconstruction of PEMFC air management system. The proposed LPV model can simplify the complex nonlinear PEMFC model simultaneously maintaining a high precision. Then, in order to restructure the faults, considering the system faults as system states to be observed, an augmented robust observer is designed. The observer also considers the disturbance and measurement noise and is designed to minimize the effect caused by these system uncertainties. According to the results, the augmented robust observer can accurately estimate the system states and the mentioned component faults in different shapes. Moreover, the oxygen stoichiometry estimator is designed taking consideration of system fault information and a simple-structure controller is employed for air compressor voltage following the net power maximization strategy. In this work, two faults are discussed, which cannot cover all possible system failures. So in the future, we decide to study the complete fault diagnosis system of the fuel cell system and are committed to optimize the accuracy and applicability of the current fault observers.

Acknowledgement

This work is supported by the National Natural Science Foundation of China (Grant No. 61803359).

Appendix

1. Verification of the Assumptions in 2.2.

The output matrix C in Eq. (11) equals $\begin{bmatrix} 0 & 0 & 1 & 0 & 0 & 0 \\ 0 & 0 & 0 & 1 & 0 & 0 \\ 0 & 0 & 0 & 0 & 0 & 1 \end{bmatrix}$,

which is full row rank. E is a unit matrix, so $\text{rank} \begin{bmatrix} E \\ C \end{bmatrix} = 6$.

Matrices F_i , $i = 1, \dots, h$, which $h = 7$ (total 7 operating points, the current from 90A to 270A), are obtained by linearization. The values are shown as follows:

$$F_1 = \begin{bmatrix} -0.1720 & 1.6437 \\ -1.0311 & 5.2442 \\ -0.0049 & -0.4764 \\ -0.0103 & -0.4910 \\ -0.1484 & -7.0992 \\ -1.5503 & 0.1423 \end{bmatrix}, \quad F_2 = \begin{bmatrix} -0.1783 & 1.6312 \\ -1.0843 & 5.1962 \\ -0.0061 & -0.5662 \\ -0.0113 & -0.5162 \\ -0.1555 & -7.1133 \\ -1.5693 & 0.1426 \end{bmatrix}, \quad F_3 = \begin{bmatrix} -0.1790 & 1.6224 \\ -1.1253 & 5.1561 \\ -0.0060 & -0.5393 \\ -0.0121 & -0.5378 \\ -0.1604 & -7.1014 \\ -1.5803 & 0.1426 \end{bmatrix}, \quad F_4 = \begin{bmatrix} -0.1777 & 1.6151 \\ -1.1589 & 5.1205 \\ -0.0061 & -0.5386 \\ -0.0129 & -0.5575 \\ -0.1642 & -7.0933 \\ -1.5889 & 0.1424 \end{bmatrix},$$

$$F_5 = \begin{bmatrix} -0.1744 & 1.6089 \\ -1.1853 & 5.0882 \\ -0.0061 & -0.5227 \\ -0.01356 & -0.5761 \\ -0.1671 & -7.0945 \\ -1.5904 & 0.1420 \end{bmatrix}, \quad F_6 = \begin{bmatrix} -0.1709 & 1.60312 \\ -1.2064 & 5.0586 \\ -0.0055 & -0.4701 \\ -0.0142 & -0.5939 \\ -0.1694 & -7.1061 \\ -1.5907 & 0.1415 \end{bmatrix}, \quad F_7 = \begin{bmatrix} -0.1680 & 1.5971 \\ -1.2244 & 5.0296 \\ -0.0044 & -0.3725 \\ -0.0147 & -0.6122 \\ -0.1715 & -7.1224 \\ -1.5909 & 0.1409 \end{bmatrix}.$$

It is easily calculated that matrices F_i , $i = 1, \dots, h$, are of full column rank.

2. Proof of Theorem 1.

In order to prove the stability and convergence of the proposed LPV-based observer in section [The fault diagnosis algorithm](#), the Lyapunov-based method is applied.

The Lyapunov function is chosen as:

$$V(k) = \mathbf{e}^T(k)P\mathbf{e}(k), P > 0 \quad (39)$$

Define a criterion function, as shown in Eq. (40):

$$J = \sum_{k=0}^{\infty} (\Delta V(k) + \mathbf{e}^T(k)\mathbf{e}(k) - \gamma_d^2 \mathbf{w}^T(k)\mathbf{w}(k) - \gamma_f^2 \Delta \mathbf{f}^T(k)\Delta \mathbf{f}(k) - \gamma_{v1}^2 \mathbf{v}^T(k)\mathbf{v}(k) - \gamma_{v2}^2 \mathbf{v}^T(k+1)\mathbf{v}(k+1)) \quad (40)$$

So if the following inequality is true for all time k :

$$\Delta V(k) + \mathbf{e}^T(k)\mathbf{e}(k) - \gamma_d^2 \mathbf{w}^T(k)\mathbf{w}(k) - \gamma_f^2 \Delta \mathbf{f}^T(k)\Delta \mathbf{f}(k) - \gamma_{v1}^2 \mathbf{v}^T(k)\mathbf{v}(k) - \gamma_{v2}^2 \mathbf{v}^T(k+1)\mathbf{v}(k+1) < 0 \quad (41)$$

$$\begin{aligned} & \Delta V(k) + \mathbf{e}^T(k)\mathbf{e}(k) - \gamma_d^2 \mathbf{w}^T(k)\mathbf{w}(k) - \gamma_f^2 \Delta \mathbf{f}^T(k)\Delta \mathbf{f}(k) - \gamma_{v1}^2 \mathbf{v}^T(k)\mathbf{v}(k) - \gamma_{v2}^2 \mathbf{v}^T(k+1)\mathbf{v}(k+1) \\ &= \left\{ \sum_{i=1}^h \rho_i(\theta(k)) (T\bar{G}_i - L_i \bar{C})\mathbf{e}(k) + T\bar{D}_i \mathbf{w}(k) + T\bar{K}_i \Delta \mathbf{f}(k) - L_i \mathbf{v}(k) - N\mathbf{v}(k+1) \right\}^T P \\ & \times \left\{ \sum_{i=1}^h \rho_i(\theta(k)) (T\bar{G}_i - L_i \bar{C})\mathbf{e}(k) + T\bar{D}_i \mathbf{w}(k) + T\bar{K}_i \Delta \mathbf{f}(k) - L_i \mathbf{v}(k) - N\mathbf{v}(k+1) \right\} \\ & - \mathbf{e}^T(k)P\mathbf{e}(k) + \mathbf{e}^T(k)\mathbf{e}(k) - \gamma_d^2 \mathbf{w}^T(k)\mathbf{w}(k) - \gamma_f^2 \Delta \mathbf{f}^T(k)\Delta \mathbf{f}(k) - \gamma_{v1}^2 \mathbf{v}^T(k)\mathbf{v}(k) - \gamma_{v2}^2 \mathbf{v}^T(k+1)\mathbf{v}(k+1) \quad (42) \\ & \triangleq \begin{bmatrix} \mathbf{e}(k) \\ \mathbf{w}(k) \\ \Delta \mathbf{f}(k) \\ \mathbf{v}(k) \\ \mathbf{v}(k+1) \end{bmatrix}^T \begin{bmatrix} \Lambda_1^T P \Lambda_1 - P + C_f^T C_f & \Lambda_1^T P \Lambda_2 & \Lambda_1^T P \Lambda_3 & -\Lambda_1^T P \Lambda_4 & -\Lambda_1^T P \Lambda_5 \\ * & \Lambda_2^T P \Lambda_2 - \gamma_d^2 I_{n_x} & \Lambda_2^T P \Lambda_3 & -\Lambda_2^T P \Lambda_4 & -\Lambda_2^T P \Lambda_5 \\ * & * & \Lambda_3^T P \Lambda_3 - \gamma_f^2 I_{n_x} & -\Lambda_3^T P \Lambda_4 & -\Lambda_3^T P \Lambda_5 \\ * & * & * & \Lambda_4^T P \Lambda_4 - \gamma_{v1}^2 I_{n_u} & -\Lambda_4^T P \Lambda_5 \\ * & * & * & * & \Lambda_5^T P \Lambda_5 - \gamma_{v2}^2 I_{n_v} \end{bmatrix} \begin{bmatrix} \mathbf{e}(k) \\ \mathbf{w}(k) \\ \Delta \mathbf{f}(k) \\ \mathbf{v}(k) \\ \mathbf{v}(k+1) \end{bmatrix} < 0 \end{aligned}$$

where $A_1 = \sum_{i=1}^h \rho_i(\theta(k))(T\bar{G}_i - L_i\bar{C})$, $A_2 = \sum_{i=1}^h \rho_i(\theta(k))(T\bar{D}_i)$, $A_3 = \sum_{i=1}^h \rho_i(\theta(k))(T\bar{K}_i)$, $A_4 = \sum_{i=1}^h \rho_i(\theta(k))L_i$ and $A_5 = \sum_{i=1}^h \rho_i(\theta(k))N$.

From Eq. (42), if the intermediate matrix is negative, then Eq. (29) is true. According to the Schur complement lemma and nature of weighting factor $\rho_i(\theta(k))$, the inequality (41) is equal to

- [10] Han IS, Chung CB. A hybrid model combining a support vector machine with an empirical equation for predicting polarization curves of PEM fuel cells. *Int J Hydrogen Energy* 2017;42(10):7023–8.
- [11] Chen J, Liu Z, Wang F, et al. Optimal oxygen excess ratio control for PEM fuel cells. *IEEE Trans Contr Syst Technol* 2017;26(5):1711–21.
- [12] Olteanu SC, Aitouche A, Oueidat M, et al. PEM fuel cell modeling and simulation via the takagi-sugeno fuzzy model [C]//2012 international Conference on renewable Energies for developing countries (REDEC). IEEE 2012:1–7.

$$\begin{bmatrix} -P + C_f^T C_f & 0 & 0 & 0 & 0 & (T\bar{G}_i - L_i\bar{C})^T P \\ * & -\gamma_d^2 I_{n_x} & 0 & 0 & 0 & (T\bar{D}_i)^T P \\ * & * & -\gamma_f^2 I_{n_f} & 0 & 0 & (T\bar{K}_i)^T P \\ * & * & * & -\gamma_{v1}^2 I_{n_u} & 0 & -L_i^T P \\ * & * & * & * & -\gamma_{v2}^2 I_{n_u} & -N^T P \\ * & * & * & * & * & -P \end{bmatrix} < 0, \quad i = 1, 2, \dots, h \quad (43)$$

Substitute the definition (25)–(28) and let $W_i = P^{-1}L_i$, then Eq. (43) can be rewritten as the LMI group in Theorem 1. Therefore the proposed observer is proven to have the advantages of stability and robustness.

REFERENCES

- [1] Li X, Wang Y, Yang D, et al. Adaptive energy management strategy for fuel cell/battery hybrid vehicles using Pontryagin's Minimal Principle. *J Power Sources* 2019;440:227105.
- [2] Deng H, Li Q, Cui Y, et al. Nonlinear controller design based on cascade adaptive sliding mode control for PEM fuel cell air supply systems. *Int J Hydrogen Energy* 2019;44(35):19357–69.
- [3] Yang D, Pan R, Wang Y, et al. Modeling and control of PEMFC air supply system based on TS fuzzy theory and predictive control. *Energy*; 2019. p. 116078.
- [4] Rasheed RKA, Liao Q, Caizhi Z, et al. A review on modelling of high temperature proton exchange membrane fuel cells (HT-PEMFCs). *Int J Hydrogen Energy* 2017;42(5):3142–65.
- [5] Pukrushpan JT, Stefanopoulou AG, Peng H. Control of fuel cell power systems: principles, modeling, analysis and feedback design. Springer Science & Business Media; 2004.
- [6] Ziogou C, Voutetakis S, Georgiadis MC, et al. Model predictive control (MPC) strategies for PEM fuel cell systems—A comparative experimental demonstration. *Chem Eng Res Des* 2018;131:656–70.
- [7] Xu L, Fang C, Hu J, et al. Parameter extraction and uncertainty analysis of a proton exchange membrane fuel cell system based on Monte Carlo simulation. *Int J Hydrogen Energy* 2017;42(4):2309–26.
- [8] Restrepo C, Konjedic T, Guarnizo C, et al. Simplified mathematical model for calculating the oxygen excess ratio of a PEM fuel cell system in real-time applications. *IEEE Trans Ind Electron* 2013;61(6):2816–25.
- [9] da Costa Lopes F, Watanabe EH, Rolim LGB, et al. A control-oriented model of a PEM fuel cell stack based on NARX and NOE neural networks. *IEEE Trans Ind Electron* 2015;62(8):5155–63.
- [10] Rotondo D, Fernandez-Canti RM, Tornil-Sin S, et al. Robust fault diagnosis of proton exchange membrane fuel cells using a Takagi-Sugeno interval observer approach. *Int J Hydrogen Energy* 2016;41(4):2875–86.
- [11] Li S, Aitouche A, Wang H, et al. Sensor fault estimation of PEM fuel cells using Takagi Sugeno fuzzy model. *Int J Hydrogen Energy* 2019. <https://doi.org/10.1016/j.ijhydene.2019.01.100>.
- [12] Chatrattanawet N, Hakhen T, Kheawhom S, et al. Control structure design and robust model predictive control for controlling a proton exchange membrane fuel cell. *J Clean Prod* 2017;148:934–47.
- [13] De Lira S, Puig V, Quevedo J, et al. LPV observer design for PEM fuel cell system: application to fault detection. *J Power Sources* 2011;196(9):4298–305.
- [14] De Lira S, Puig V, Quevedo J. LPV model-based fault diagnosis using relative fault sensitivity signature approach in a PEM fuel cell. *IFAC Proceed Vol* 2009;42(8):528–33.
- [15] Bougatf Z, Abdelkrim N, Aitouche A, et al. Fault detection of a PEMFC system based on delayed LPV observer. *Int J Hydrogen Energy* 2018. <https://doi.org/10.1016/j.ijhydene.2018.11.053>.
- [16] Pahon E, Steiner NY, Jemei S, et al. A signal-based method for fast PEMFC diagnosis. *Appl Energy* 2016;165:748–58.
- [17] Zheng Z, Péra MC, Hissel D, et al. A double-fuzzy diagnostic methodology dedicated to online fault diagnosis of proton exchange membrane fuel cell stacks. *J Power Sources* 2014;271:570–81.
- [18] Lee YH, Kim J, Yoo S. On-line and real-time diagnosis method for proton membrane fuel cell (PEMFC) stack by the superposition principle. *J Power Sources* 2016;326:264–9.
- [19] Mao L, Jackson L, Huang W, et al. Polymer electrolyte membrane fuel cell fault diagnosis and sensor abnormality identification using sensor selection method. *J Power Sources* 2020;447:227394.
- [20] Li Z, Outbib R, Giurgea S, et al. Fault detection and isolation for polymer electrolyte membrane fuel cell systems by analyzing cell voltage generated space. *Appl Energy* 2015;148:260–72.
- [21] Li Z, Outbib R, Giurgea S, et al. Fault diagnosis for PEMFC systems in consideration of dynamic behaviors and spatial inhomogeneity. *IEEE Trans Energy Convers* 2018;34(1):3–11.

- [25] Kim J, Lee I, Tak Y, et al. State-of-health diagnosis based on hamming neural network using output voltage pattern recognition for a PEM fuel cell. *Int J Hydrogen Energy* 2012;37(5):4280–9.
- [26] Hua J, Li J, Ouyang M, et al. Proton exchange membrane fuel cell system diagnosis based on the multivariate statistical method. *Int J Hydrogen Energy* 2011;36(16):9896–905.
- [27] Liu J, Li Q, Chen W, et al. A discrete hidden Markov model fault diagnosis strategy based on K-means clustering dedicated to PEM fuel cell systems of tramways. *Int J Hydrogen Energy* 2018;43(27):12428–41.
- [28] Liu J, Li Q, Yang H, et al. Sequence fault diagnosis for PEMFC water management subsystem using deep learning with t-SNE. *IEEE Access* 2019;7:92009–19.
- [29] Lee WY, Oh H, Kim M, et al. Hierarchical fault diagnostic method for a polymer electrolyte fuel cell system. *Int J Hydrogen Energy* 2019. <https://doi.org/10.1016/j.ijhydene.2019.10.145>.
- [30] Kamal E, Aitouche A. Fuzzy observer-based fault tolerant control against sensor faults for proton exchange membrane fuel cells. *Int J Hydrogen Energy* 2018. <https://doi.org/10.1016/j.ijhydene.2018.10.070>.
- [31] Laghrouche S, Liu J, Ahmed FS, et al. Adaptive second-order sliding mode observer-based fault reconstruction for PEM fuel cell air-feed system. *IEEE Trans Contr Syst Technol* 2015;23(3):1098–109.
- [32] Escobet T, Feroldi D, De Lira S, et al. Model-based fault diagnosis in PEM fuel cell systems. *J Power Sources* 2009;192(1):216–23.
- [33] Liu J, Luo W, Yang X, et al. Robust model-based fault diagnosis for PEM fuel cell air-feed system. *IEEE Trans Ind Electron* 2016;63(5):3261–70.
- [34] Vijay P, Tadé MO, Shao Z. Adaptive observer based approach for the fault diagnosis in solid oxide fuel cells. *J Process Contr* 2019;84:101–14.
- [35] Chen K, Laghrouche S, Djerdir A. Fuel cell health prognosis using Unscented Kalman Filter: postal fuel cell electric vehicles case study. *Int J Hydrogen Energy* 2019;44(3):1930–9.
- [36] Han J, Yu S, Sun Y. Oxygen excess ratio control for proton exchange membrane fuel cell using model reference adaptive control. *Int J Hydrogen Energy* 2019;44(33):18425–37.
- [37] Hsu PL, Houng YC, Yeh SS. Design of an optimal unknown input observer for load compensation in motion systems. *Asian J Contr* 2001;3(3):204–15.
- [38] Sankar K, Jana AK. Nonlinear multivariable sliding mode control of a reversible PEM fuel cell integrated system. *Energy Convers Manag* 2018;171:541–65.